Research Square

Preprints are preliminary reports that have not undergone peer review.
They should not be considered conclusive, used to inform clinical practice,
or referenced by the media as validated information.

Supersoft yet tough bottlebrush polymers via dynamic domain exchange

Jiheong Kang

jiheongkang@snu.ac.kr

Seoul National University https://orcid.org/0000-0003-4446-5494

Hyunjun Kim

Seoul National University https://orcid.org/0000-0001-8861-0206

Yeonzu Son

Korea Advanced Institute of Science and Technology

Jaeho Lee

Seoul National University https://orcid.org/0000-0001-7584-920X

Ji Woong Yu

Korea Institute for Advanced Study

Intanon Lapkriengkri

University of California, Santa Barbara

Byeongdu Lee

Argonne National Laboratory https://orcid.org/0000-0003-2514-8805

YongJoo Kim

Korea University https://orcid.org/0000-0002-6037-7243

Seongjun Park

Seoul National University https://orcid.org/0000-0002-1981-9628

Christopher M. Bates

University of California, Santa Barbara

Article

Keywords:

Posted Date: March 12th, 2026

DOI: https://doi.org/10.21203/rs.3.rs-9046391/v1

License: This work is licensed under a Creative Commons Attribution 4.0 International License.
Read Full License

Additional Declarations: There is **NO** Competing Interest.

Supersoft yet tough bottlebrush polymers via dynamic domain exchange

Hyunjun Kim[1†], Yeonzu Son[2†], Jaeho Lee[1†], Ji Woong Yu[3†], Intanon Lapkriengkri[4], Byeongdu Lee[5], YongJoo Kim[6]*, Seongjun Park[7,8]*, Christopher M. Bates[4]*, and Jiheong Kang[1]*

[1] Department of Chemistry, Seoul National University, Seoul, 08826, Republic of Korea

[2] Program of Brain and Cognitive Engineering, Korea Advanced Institute of Science and Technology, Daejeon, 34141, Republic of Korea

[3] Korea Institute for Advanced Study, Seoul, 02455, Republic of Korea

[4] Materials Department, University of California, Santa Barbara, CA, 93106, USA

[5] X-ray Science Division, Advanced Photon Source, Argonne National Laboratory, Lemont, IL, 60439, USA

[6] Department of Materials Science and Engineering, Korea University, Seoul, 02841, Republic of Korea

[7] School of Transdisciplinary Innovations, Seoul National University, Seoul, 08826, Republic of Korea

[8] Medical Research Center, Seoul National University, Seoul, 03080, Republic of Korea

†These authors equally contributed to this work

*To whom correspondence should be addressed:
E-mail: jiheongkang@snu.ac.kr, cbates@ucsb.edu, seongjunpark@snu.ac.kr, cjyjee@korea.ac.kr

Abstract

Biological tissues exhibit a unique combination of supersoft mechanics and high toughness, a property pairing rarely achieved in synthetic solids. Replicating this duality in solvent-free synthetic polymers remains a fundamental challenge, as the strategies required for supersoftness and high toughness are inherently incompatible. Here, we present a bottlebrush polymer design strategy featuring unique dynamic domain exchange behavior that simultaneously achieves tissue-level softness and high fracture toughness. Our BBPs form physically crosslinked, dynamic networks with suppressed entanglements and dynamic domain exchange under deformation, allowing rapid network reconstruction and efficient energy dissipation under strain. As a result, the material exhibits tissue-like softness ($E \approx 40$ kPa), ultra-high stretchability (~1,300%), and exceptional toughness (~9,300 J m^{-2}). This unique combination enables conformal yet mechanically robust integration with biological tissue, significantly reducing foreign-body responses and sustaining long-term *in vivo* stability.

Introduction

Developing tissue-like polymeric materials is critical for advancing bioimplantable technologies[1–5]. Seamless integration with biological systems requires synthetic implants to replicate the supersoftness and deformability of native tissues, minimizing foreign-body responses and mechanical mismatch at the interface[6]. However, a significant disparity persists between biological tissues (Young's modulus: 10–100 kPa) and synthetic polymers (rubbers: ~1 MPa; plastics: ~1 GPa)[4,7]. Achieving moduli below ~100 kPa in synthetic polymer is inherently difficult due to intrinsic polymer chain entanglements and interchain interactions (Fig. 1a, top)[8,9]. The conventional solution involves incorporating solvents, such as water, to form gels, thereby swelling the network and reducing both its crosslink density and interchain interactions[10]. While this method successfully lowers the modulus, it compromises environmental and long-term stability, including swelling–deswelling behavior and associated changes in surface and mechanical properties[4].

A viable solution for creating "super-soft" yet solvent-free polymers involve the use of nonlinear polymer architectures[9]. For example, bottlebrush elastomers comprise long polymeric side chains attached to a polymeric backbone. These sterically bulky side chains effectively reduce chain entanglements. Both experimental and theoretical studies have demonstrated that optimizing the combinations of backbone and side-chain molecular weights can amplify these effects[11], lowering the Young's modulus to the range of gels while remaining free of solvents or small-molecule impurities. Nevertheless, a major challenge remains: the

fundamental tradeoff between supersoftness and toughness in bottlebrush polymers. The absence of chain entanglements, together with the short backbone length, renders these materials intrinsically brittle (Fig. 1a, bottom), with fracture toughness typically below 100 J m^{-2}, which severely limits their applications[9,11–15]. While established strategies from linear polymer mechanics, such as incorporating energy-dissipating motifs[16–20] or stress-deconcentrating structures[21–23] at various length scales, can toughen bottlebrush networks, such approaches inevitably increase the modulus[24]. Consequently, simultaneously achieving tissue-level softness and high toughness in synthetic polymers without solvent remains a fundamental challenge.

Here, to address this challenge, we present a design strategy for bottlebrush polymers (BBPs) that self-assemble to create strain-adaptive physical crosslinks that can reorganize and recover under applied loads (Fig. 1b). This BBP design enhances stretchability, strength, and toughness while maintaining supersoftness by enabling rapid dissociative–associative exchange among domains without irreversible destruction of the network. The unique combination of physical crosslinking and molecular reconfigurability overcomes the inherent tradeoff between modulus and toughness. Operating without solvent, an optimal BBP network with this design achieved high stretchability (>1,300%) and high fracture toughness (~9,300 J m^{-2}) while retaining tissue-like softness of $E \approx 40$ kPa (Fig. 1c). The resulting toughness is comparable to that of tough biological tissues and even state-of-the-art synthetic hydrogels. The advantage of this softness–toughness combination is evident from in vivo implantation experiments, where conformal and mechanically robust tissue integration with tissue suppressed foreign-body

responses (Fig. 1d). In summary, this material platform creates opportunities in both fundamental and applied polymer science for the design of soft materials with unique properties.

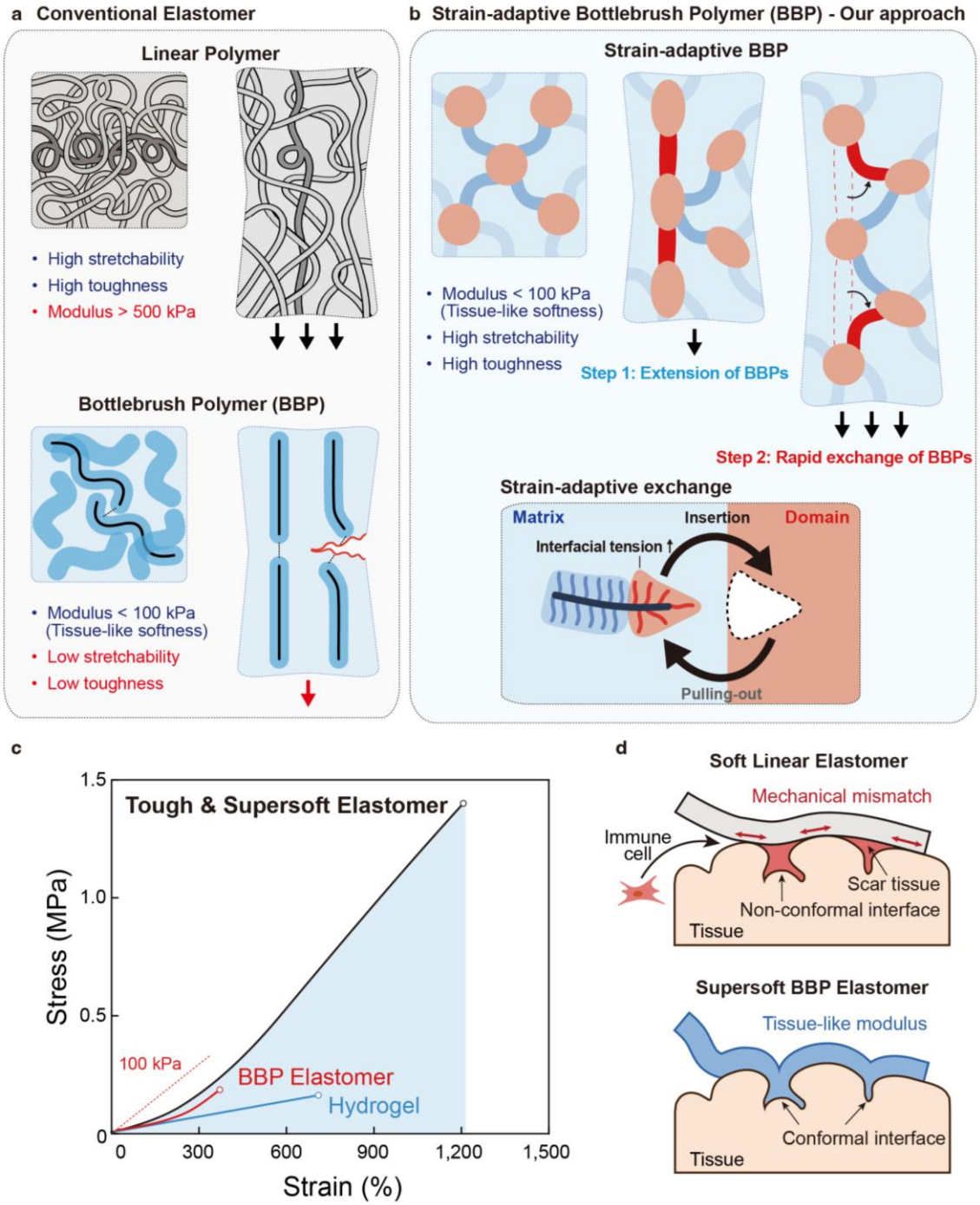


Fig. 1: Tough and supersoft elastomer.

a, Schematic illustration of network structure and intrinsic properties of the conventional elastomers. **b,** Schematic illustration of tough BBP elastomer network and the unique toughening mechanism. Network reconstruction through the dynamic exchange of crosslinking domains overcomes the intrinsic limitations of the BBP network. **c,** Stress-strain behavior of ideal tissue-like soft materials. **d,** Schematic illustration of the critical difference between "soft" and "supersoft" in bioimplant applications.

Design, synthesis, and self-assembly of triblock bottlebrush polymers (BBPs)

We designed and synthesized a triblock BBP via ring-opening metathesis polymerization (ROMP) of norbornene-based macromonomers bearing two distinct side chains (Fig. 2a, left and Supplementary Fig. 1). The first and third blocks were appended with polystyrene (PS) side chains ($M_n \approx 2.5$ kg mol^{-1}) with a backbone degree of polymerization (DP) of 12, respectively, whereas poly(ethylene glycol) (PEG) ($M_n \approx 0.5$ kg mol^{-1}) was attached to the middle block with a backbone DP of 360. The structure of the BBPs were characterized by ^{1}H nuclear magnetic resonance (NMR) spectroscopy (Supplementary Fig. 2), as well as by gel permeation chromatography (GPC) (Supplementary Fig. 3). The analyses revealed number-average molecular weights (M_n) of 219 kg mol^{-1} with low molar-mass dispersities ($Đ$ = 1.06). Owing to the large interaction parameter between PS and PEG[25] and the PS volume fraction of approximately 20%, the resultant triblock BBPs form distinct spherical physically crosslinked

domains composed of PS blocks (Fig. 2a, right). These crosslinking domains provide the network with sufficient mechanical integrity to yield a transparent, free-standing film. In contrast, the corresponding homo-bottlebrush analogues—BBP-PS and BBP-PEG—failed to form free-standing films, owing to their weak intermolecular interactions and the short contour length of their backbones (Supplementary Fig. 4). Differential scanning calorimetry (DSC) is consistent with microphase separation, showing two glass transition temperatures (T_g): glassy PS-based crosslinks (T_g = 87 °C) embedded in a rubbery PEG-based matrix (T_g = -56 °C) on the second heating ramp (Supplementary Fig. 5). The structure of the physically crosslinked network was further investigated with small angle X-ray scattering (SAXS) measurements (Supplementary Fig. 6). 2D SAXS images revealed isotropic diffraction rings corresponding to a lattice of $\boldsymbol{q}$ = 0.018 $Å^{-1}$ and features consistent with a spherical form factor. By analyzing the corresponding 1D profiles, we confirmed the presence of spherical domains with a radius of 18 nm and a domain surface-to-surface distance of 16 nm, which is shorter than the BBP-PEG backbone contour length (~90 nm) (Fig. 2b and Supplementary Fig. 7). BBP chains therefore adopt a bent configuration. This microstructure was also confirmed by TEM analysis (Fig. 2b, inset and Supplementary Fig. 8).

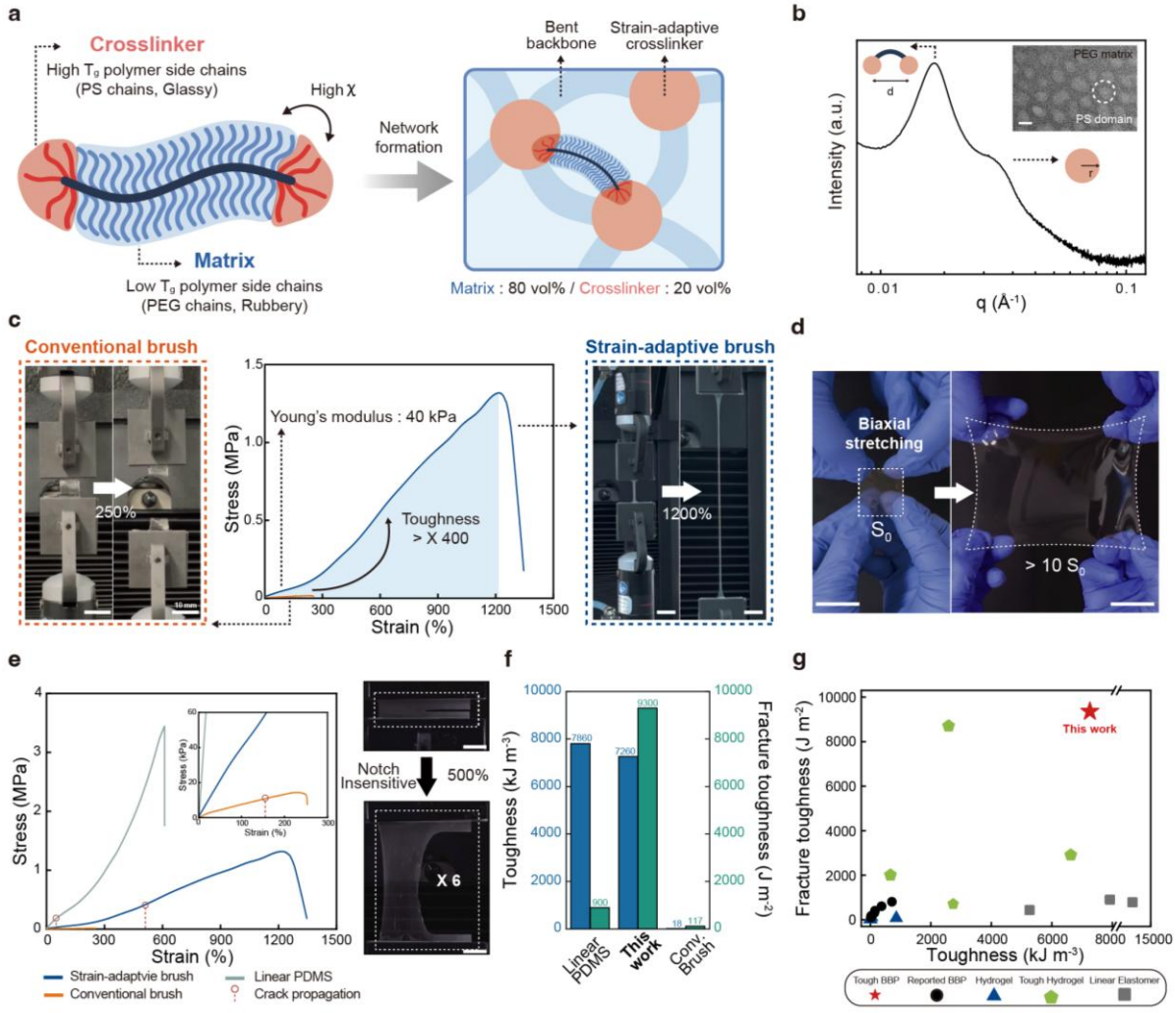


Fig. 2: Mechanical properties of strain-adaptive BBP network.

a, Schematic illustration of the polymer and network structure of strain-adaptive BBP network. **b,** SAXS profile of the strain-adaptive BBP network and TEM image (inset). **c,** Stress-strain curve and photographs of a conventional BBP network and highly stretchable strain-adaptive BBP network. Scale bars, 10 mm. **d,** Photographs showing more than 10 times dimensional expansion of the strain-adaptive BBP network. Scale bars, 3 cm. **e,** Stress-strain curve and fracture properties of linear PDMS, conventional BBP, and strain-adaptive BBP elastomers (left),

and photographs demonstrating notch insensitive stretching of the strain-adaptive BBP network (right). Scale bars, 10 mm. **f,** Toughness and fracture toughness of the three elastomers. **g,** Comparison of toughness and fracture toughness among soft elastomers with low Young's modulus (< 300 kPa)[10,11,16,17,21,22].

Mechanical properties of triblock BBPs

Uniaxial tensile tests on our BBP films indicated that they are supersoft ($E \approx 40$ kPa) and can be stretched up to 13 times their initial length before failure (Fig. 2c). Remarkably, despite this tissue-level softness and extreme stretchability, the BBPs exhibit record-high fracture strength ($\sigma_f \sim 1.3$ MPa) with pronounced hyperelastic behavior—distinct from reported supersoft BBPs (σ_f < 300 kPa)[11–15,26]. Biaxial stretching experiments are broadly consistent with the mechanical toughness measured in uniaxial tension, with dimensional expansion exceeding 10× before failure (Fig. 2d). Furthermore, in notch tests, the BBP shows excellent fracture toughness ($\Gamma \sim 9{,}300$ J m^{-2}) and notch insensitivity, as even notched samples sustain a stretch ratio of 6 (Fig. 2e,f). To the best of our knowledge, this is the only system that simultaneously achieves high toughness and fracture properties among networks with soft tissue-like modulus (E < 300 kPa) (Fig. 2e-g and Supplementary Figs. 9 and 10). Given the short contour length and absence of sacrificial bonds available in the network for energy dissipation, an obvious question is why these BBPs achieve such an unusual combination of softness, high stretchability, and high fracture toughness?

To achieve supersoftness, both the interactions among BBPs and the entanglements within the network must be minimized. For this purpose, the lengths of the side chains and backbone are crucial parameters that affect inter-brush interactions and determine their flexibility. To systematically study these effects, we synthesized a series of BBPs and investigated their stress-strain behaviors (Supplementary Table 1). First, we varied the length of the BBP side chains (Supplementary Fig. 11). The BBP with shorter side chains ($M_n \approx 0.1$ kg mol^{-1}, length ≈ 1.1 nm) exhibited a higher modulus ($E \approx 200$ kPa), indicating stronger inter-brush interactions and entanglements. In contrast, BBPs with longer side chains ($M_n \approx 4.0$ kg mol^{-1}, length ≈ 7.9 nm) (Supplementary Fig. 12) also showed a high modulus but with brittleness[25] (Supplementary Fig. 11c). The long side chains began to crystallize, turning the BBPs into rigid structures despite the reduced inter-brush interactions and entanglements. Achieving tissue-like softness therefore requires both minimized inter-brush interactions and sufficient backbone flexibility, for which a side-chain length of around ~2.3 nm is optimal.

We also examined the influence of backbone length of BBPs (Supplementary Figs. 7, 13, and 14). The short backbone BBP (Backbone DP (N_{bb}) ≈ 200, length ≈ 55 nm) exhibited a relatively high modulus ($E \approx 130$ kPa), whereas a longer backbone BBP ($N_{bb} \approx 800$, length ≈ 180 nm) showed a lower modulus ($E \approx 30$ kPa) as expected. Backbone length governs the overall flexibility of BBPs. Longer backbones adopt more easily deformable, bent conformations, making them easier to extend and thereby reducing the modulus[11].

The microphase morphology is a crucial factor in determining the softness of these

BBP materials. We synthesized a series of BBPs with varying volume fractions (11 ~ 50 vol%) of PS blocks and found that to maintain the supersoftness, the rubbery block must retain at least 70% of its volume compared to the glassy blocks (Supplementary Fig. 15). Once the glassy block exceeds 30%, the modulus increases dramatically due to formation of 3D percolated glassy domains (Supplementary Fig. 16). Through systematic studies of structural components of triblock BBPs, we optimized the side chain lengths, backbone DP, and volume fraction of the crosslinking block to simultaneously achieve supersoftness and mechanical toughness.

Mechanical behavior and dynamic exchange mechanism of BBP domains

The triblock BBP system doesn't have any moieties for directional noncovalent interactions or chain entanglements, both of which typically contribute to energy dissipation and stress deconcentration. We propose that deformation of the BBP network proceeds through two distinct strain-dependent mechanisms (Fig. 3a). At low strains, deformation is governed by reversible stretching and bending of the BBP microstructure while maintaining the overall network configuration, resulting in a high degree of elasticity. Cyclic loading and unloading experiments to various strains up to 100% indicated nearly perfect elastic recovery (Supplementary Fig. 17). As monitored by the *in-situ* SAXS experiments during stretching, the scattering wave vector along the stretching direction ($\boldsymbol{q}_{//}$) decreased proportionally with an applied strain of 100% ($\boldsymbol{q}_{//,0\%} = 0.018$ Å^{-1} and $\boldsymbol{q}_{//,100\%} = 0.010$ Å^{-1}) (Supplementary Fig. 18) while the isotropic ring pattern fully recovered after release of strain (Supplementary Fig. 19).

When strain exceeds the elastic regime (>150%), the bent BBPs become fully extended and begin to release from the physical crosslinking domains. In general, this would lead to the mechanical degradation and fracture of the BBP film (Supplementary Fig. 20). Here, however, we propose that rapid BBP exchange between crosslinking domains drives continuous network reconstruction under strain, thereby enabling both high stretchability and high toughness (Fig. 3a). Consistent with this mechanism, *in-situ* SAXS measurement at a higher strain of 300% showed a non-linear decrease in $\boldsymbol{q}_{//}$ with applied strain ($\boldsymbol{q}_{//,0\%}$ = 0.018 Å^{-1}, $\boldsymbol{q}_{//,300\%}$ = 0.0064 Å^{-1}) (Supplementary Fig. 18), and neither the structure factor peak nor the form factor oscillations at higher $\boldsymbol{q}$ fully recover after releasing the strain (Supplementary Fig. 19). Despite some plastic deformations at high strains, the network still recovers to a significant extent (~30% after 300% strain, ~50% after 500% strain) (Supplementary Fig. 21).

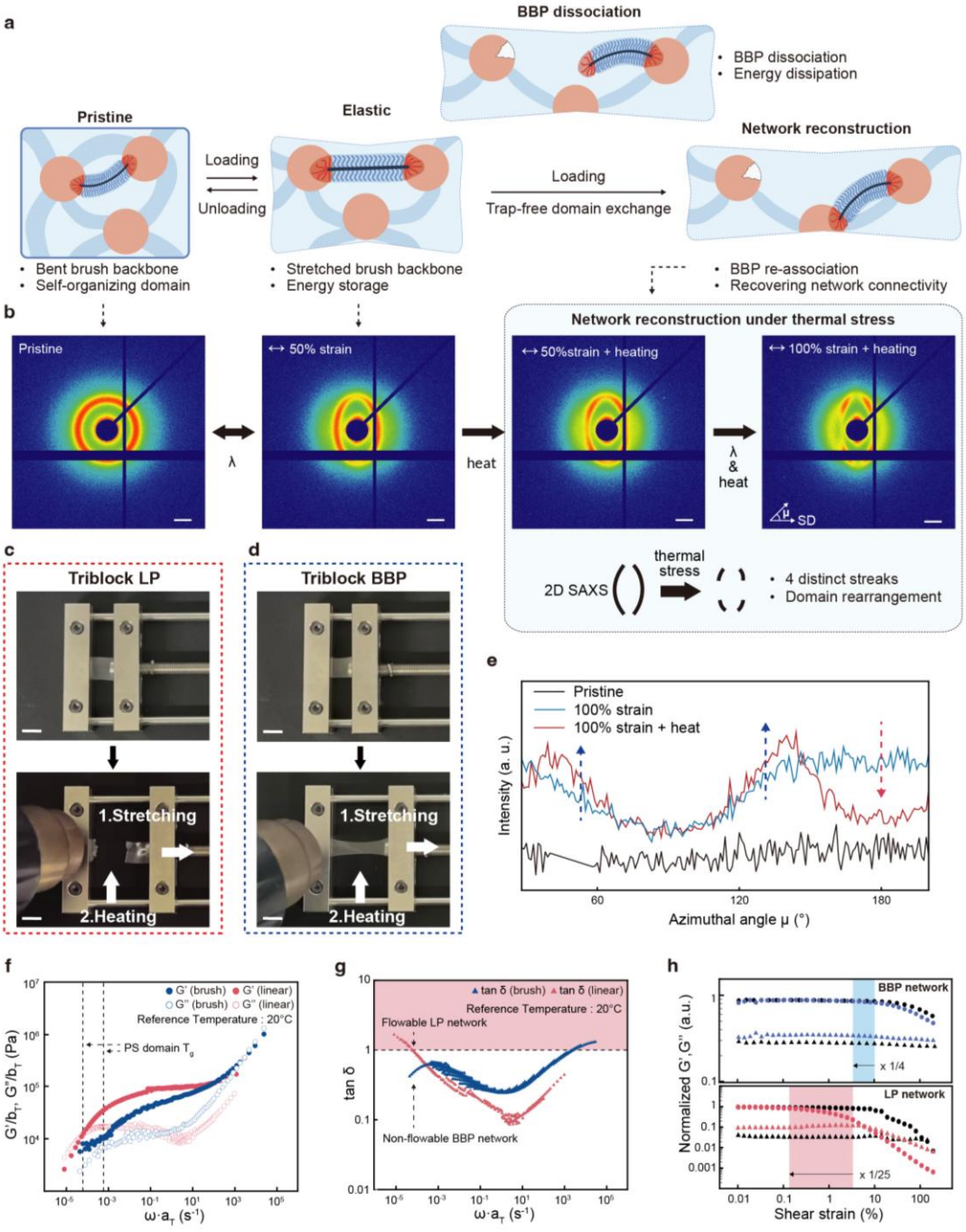


Fig. 3: Strain-adaptive behavior of BBP network.

a, Schematic illustration of the strain dependent stretching behavior of the network. Domain exchange at high strain enhances the toughness of the BBP network. **b,** 2D SAXS

images of the BBP network during stretching and subsequent heating cycles. **c,** Photographs of a stretched linear triblock SEBS film, which fails immediately upon heating and **d,** photographs of a stable strain-adaptive BBP film under the same conditions. **e,** Azimuthal angle cuts of the structural factor patterns during stretching and heating of the BBP network. The intensities at 45° and 135° increases, while the intensity at 180° decreases upon heating. **f,** TTS analysis of linear triblock copolymer and the strain-adaptive BBP network. Linear polymer network shows a crossover point near its T_g, whereas no crossover is observed for the BBP network. **g,** Loss tangent of linear triblock copolymer and the strain-adaptive BBP network. **h,** Amplitude sweep results for pristine, cyclically stretched, and released BBP films (top) and linear triblock copolymer films (bottom). (top) Filled black circles and triangles represent G' and G" of pristine BBP film, and filled blue circles and triangles represent G' and G" of stretched and released BBP film. (bottom) Filled black circles and triangles represent G' and G" of pristine linear triblock copolymer film, and filled red circles and triangles G' and G" of stretched and released linear triblock copolymer film.

We further studied the reconstruction of self-assembled BBP networks using thermal stress experiments (Supplementary Fig. 22). Thermal stress was applied to films of a pre-stretched triblock BBP films and a linear triblock copolymer, SEBS (styrene-*b*-ethylene-*co*-butylene-*b*-styrene, TUFTEC™ H1221) that possesses a similar microstructure to that of our BBP network (Supplementary Fig. 23). Thermal stress applied by a heat gun at high temperature

(150 ℃), which is above the T_g of PS crosslinks (~90 ℃), accelerates the release of polymer chains from the physically crosslinked domains, generating defects that ultimately cause fracture when the materials has been pre-strained. As expected, the linear triblock copolymer film pre-stretched to 50% fractured immediately upon exposure to high thermal stress (Fig. 3c). In contrast, the BBP film pre-stretched to 50% maintained excellent mechanical integrity even under the same conditions (Fig. 3d). This result indicates that the rapid release and re-insertion of BBP chains into crosslinked domains occurs sufficiently fast to preserve network integrity over time. By contrast, end block chains in linear triblock copolymer re-insert much more slowly, leaving a portion of released chains trapped in the matrix rather than returning to the crosslinking domains, which leads to fracture.

These results were further confirmed by X-ray analysis. In the 2D SAXS images, the BBP film stretched to a strain of 50% exhibits an oval-shaped deformation of the diffraction ring pattern. Upon applying thermal stress, the intensity along the stretching direction decreased, leaving only four distinct streaks (Fig. 3b). When the intensity is plotted as a function of the azimuthal angle, the intensity along the stretching direction (μ = 0°) decreased, whereas the intensities at specific orientations (μ = 45° and 135°) increased (Fig. 3e). This indicates that the most highly stretched BBPs dissociate from their domains and undergo network reconstruction, which effectively releases the local stress[27]. This behavior was consistently observed during repeated stretching and thermal stress cycling (Supplementary Fig. 24a). Moreover, in the case of short backbone BBPs with faster exchange kinetics, similar structural changes appear even

during mechanical stretching alone, without thermal stress (Supplementary Fig. 25). In contrast, as mentioned above, linear triblock copolymer films fail quickly under thermal stress due to their slow chain dynamics, preventing X-ray structural analysis (Supplementary Fig. 24b).

This fast dynamic exchange of triblock BBPs is driven by the high interfacial tension and the simple conformation of BBPs[28]. In contrast, LPs are aggregated to minimized surface area and flow in the matrix (Supplementary Fig. 26). Rheological analysis further supports this mechanism. In time-temperature superposition (TTS) of frequency sweep (-20 to 120 ℃), the LP network shows crossover point of G' and G" (Fig. 3f) that starts flowing (loss factor > 1) once the crosslinking domains become rubbery (Fig. 3g), whereas the BBP network retains solid-like behavior (loss factor < 1) even after the crosslinking domains begin to melt. Moreover, our BBP network maintained its connectivity even after network disruption induced by mechanical stress, as confirmed by LVER measurement following cyclic uniaxial stretching in the large strain regime (500% strain) (Fig. 3h and Supplementary Fig. 27). The LVER of the BBP network drops only to one-quarter, whereas the LP network suffers an almost two orders of magnitude decrease, underscoring the superior resilience of BBP networks in preserving network connectivity after domain disruption. Because the dynamic exchange of BBP blocks operates across various systems, including those with different polymer combinations (Supplementary Fig. 28) and domain morphologies (Supplementary Fig. 15), we demonstrate that this mechanism serves as a broadly applicable toughening strategy for block copolymer networks.

Coarse-grained molecular dynamics simulations

The structural simplicity of BBPs enables dynamic interdomain exchanges. To better understand how end-block architecture influences mechanical behavior, we performed coarse-grained molecular dynamics (CGMD) simulations. The simulations focused on the effect of architectural contrast between linear and bottlebrush designs in the terminal A blocks. To capture this effect, two model ABA triblock copolymer systems were examined: BBB and LBL, where B and L represent bottlebrush and linear blocks, respectively (Supplementary Fig. 29). Because both systems have identical block volume fractions, they exhibit similar spherical domain morphologies at equilibrium (Fig. 4a,b and Supplementary Fig. 30).

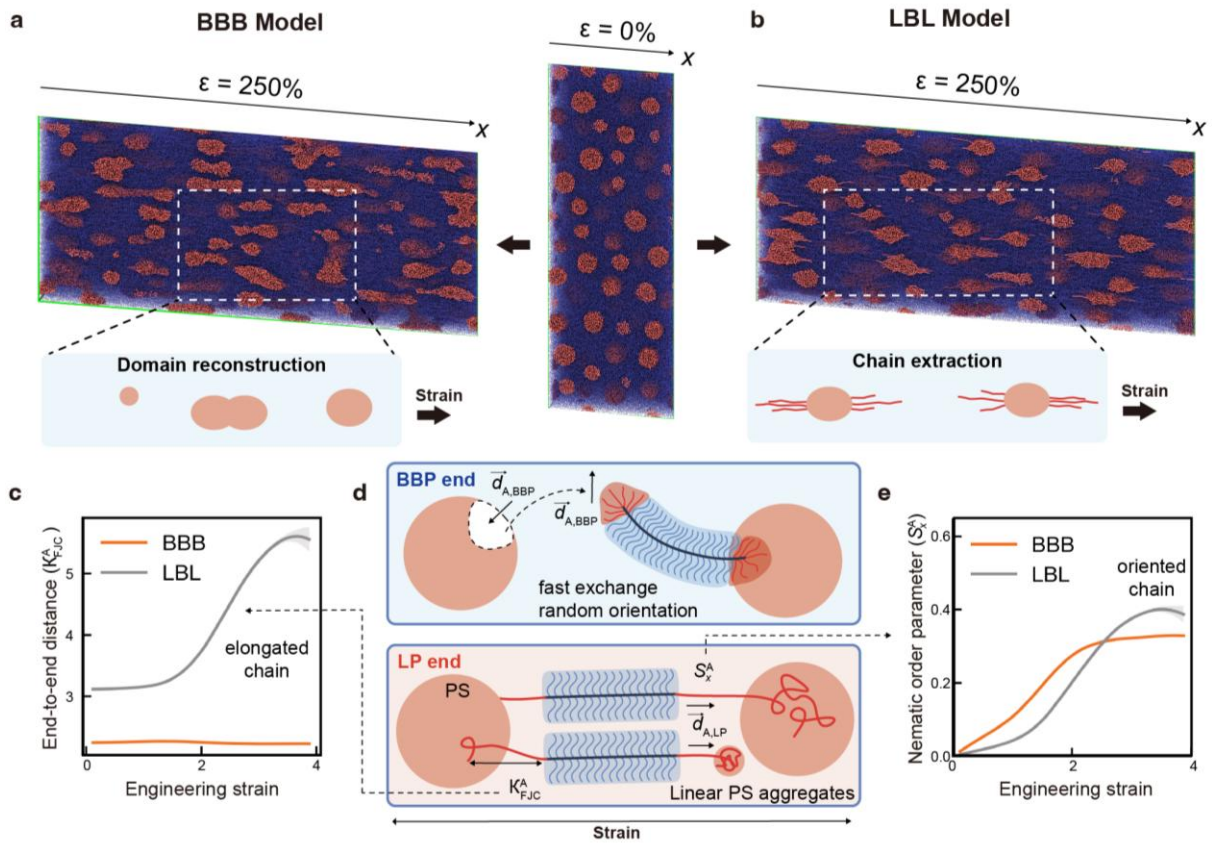


Fig. 4: CGMD simulation about the effects of end block structure.

Snapshot of the pristine and 250% stretched state of the **a,** BBB system and **b,** LBL system. **c,** Normalized end-to-end distance as a function of strain for the brush and linear end blocks in the BBB and LBL systems, respectively. **d,** Schematic illustration of brush (top) and linear (bottom) polymer end blocks under stretching. **e,** Nematic backbone order parameter as a function of strain for the brush and linear end blocks in the BBB and LBL system, respectively.

Upon uniaxial stretching, distinct structural changes were observed in the domains as quantitatively analyzed using two parameters: the normalized squared end-to-end distance of each block ($\kappa^{\alpha}_{\mathrm{FJC}}$) and backbone nematic order parameter (S^{α}_{x}) (α, FJC and x denotes A or B blocks in the ABA triblock copolymer, freely jointed chain and stretching direction, respectively) (Supplementary Fig. 31). Due to the structural differences between bundle-like BBPs and the randomly coiled LPs, the BBB domains were transformed into prolate shapes (Fig. 4a), whereas the LBL domains exhibited yarn-like extraction of LPs (Fig. 4b). Consequently, the end-to-end distance of the linear end blocks ($\kappa^{A}_{\mathrm{FJC,LBL}}$) continuously increased upon stretching, contributing only a limited degree of additional stretchability to the network (Fig. 4c). In contrast, the BBB system achieved high extensibility through dynamic exchange of bottlebrush end blocks rather than configurational changes of end blocks, as indicated by the nearly constant $\kappa^{A}_{\mathrm{FJC,BBB}}$ value during stretching.

Moreover, the backbone orientation parameter ($S^{A}_{x,BBB}$) of bottlebrush end blocks

reached saturation at ~200% strain due to reorientation through dynamic interdomain exchange of the BBPs, corresponding to the onset of plastic behavior, whereas $S_{x,LBL}^{A}$ of linear end blocks continued to increase due to progressive extraction from the domains (Fig. 4e). The structural parameters of the middle blocks ($\kappa_{\mathrm{FJC}}^{B}$ and S_{x}^{B}) were nearly identical in both systems (Supplementary Fig. 32), confirming that the pronounced differences in extensibility and toughness originate from the end block structures and their behaviors (Fig. 4d).

Tissue integration of supersoft elastomer with high toughness

Our triblock BBP system shows broad potential for biomedical implants, as it meets critical requirements for establishing a stable and safe chronic device-tissue interface: (1) high conformality, (2) high toughness, and (3) high fracture toughness (Fig. 5a). To ensure intimate integration with soft tissue and minimize foreign-body responses (FBR), implants must be mechanically compliant (Fig. 5b and Supplementary Fig. 33). However, because post-implant failure of biomedical devices can be catastrophic, they must also possess exceptional mechanical resilience, a challenge that has limited the use of supersoft materials owing to the inherent trade-off between softness and toughness (Supplementary Fig. 34). The remarkable toughness of our BBP film enables facile manipulation without fracture, even under localized strain at the grip when handled with fine-tipped surgical forceps (Fig. 5c). Moreover, the crack resistance of the BBP network allows on-demand suturing without the risk of device fracture (Fig. 5d, Supplementary Figs. 35 and 36 and Supplementary Video 1).

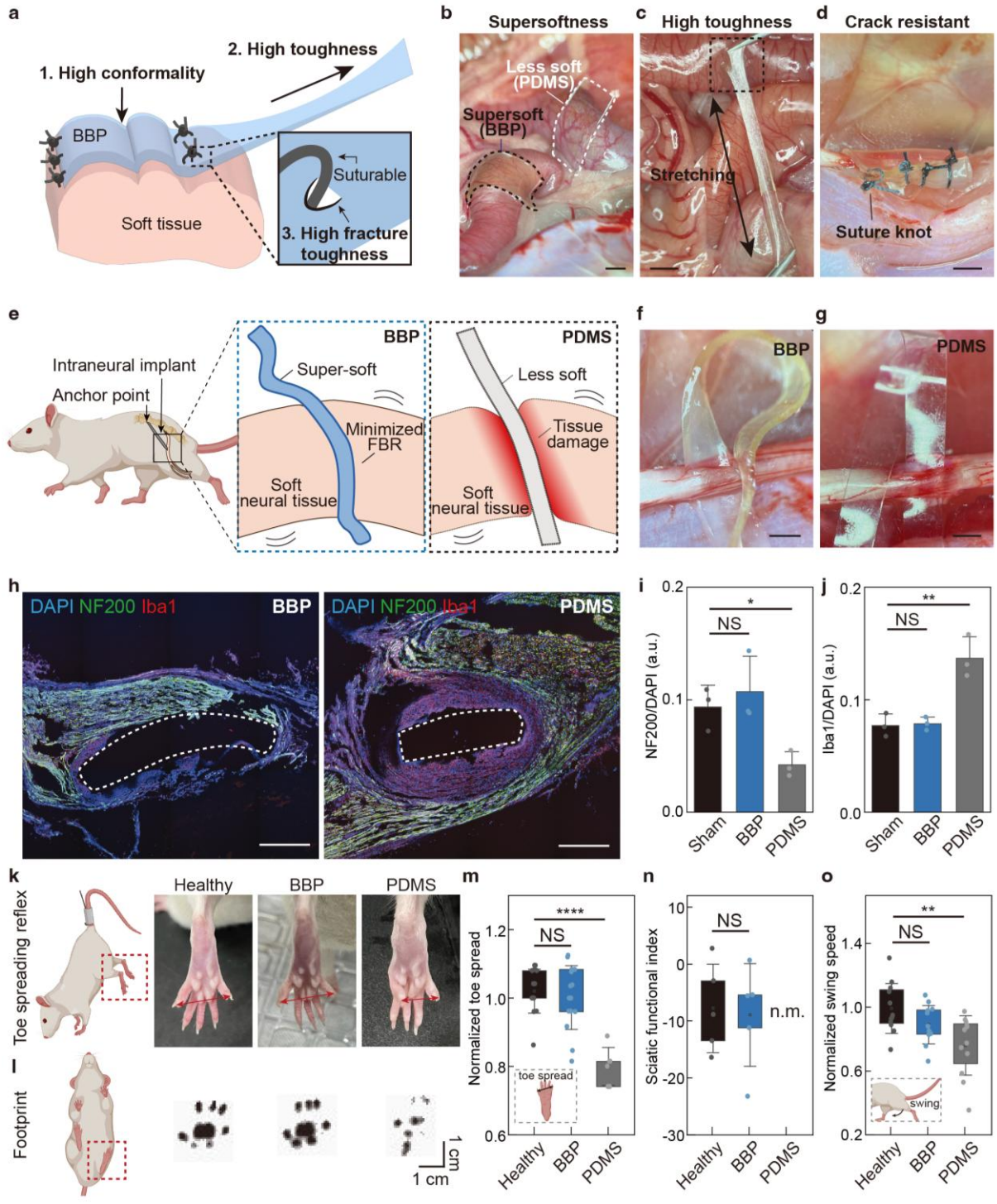


Fig. 5: Tissue-like soft and tough bioimplant.

a, Schematic illustration showing the key requirements for bioimplant substrates. **b-d,** Photographs demonstrating conformity of implants depending on substrate softness (b), high toughness of the BBP network enabling it to withstand harsh surgical handling (c) and fracture toughness of the BBP allowing on-demand suturing to the substrate without fracture (d). Scale bars, 2 mm. **e,** Schematic illustration of the effect of substrate softness on intraneural implants. **f, g,** Photographs of intraneural implant using a supersoft BBP substrate (f) and a relatively stiff PDMS substrate (g) interfacing with peripheral nerves. Scale bars, 1 mm. **h,** Confocal microscopy images of nerves implanted with BBP (left) and PDMS (right). Scale bars, 500 μm. White dashed lines represent the implant-to-tissue interfaces. **i, j,** Immunohistochemical analysis of axon viability (i) and scar tissue formation around the implants (j). **k, l,** Photographs of toe spreading reflexes (k) and representative gait footprint images (l) in healthy (non-operative), BBP-implanted, PDMS-implanted rats after 2-week implantation. **m,** Normalized toe spread. **n,** Sciatic functional index. **o,** Normalized swing speed for the three experimental groups. n.m.; not measurable due to missing toe prints. Values in (i) and (j) represent the means and SD (n=3, n is the number of animals). P values are 0.56 and 0.016 in (i); they are 0.83 and 0.0086 in (j), for BBP and PDMS, respectively. Values in (m), (n), and (o) represent the 25th and 75th percentiles ± SD. In (m) and (n), n = 15 for healthy and BBP groups (3 normal gait tracks from each of 5 animals). For PDMS in (m), n = 6 (3 normal gait tracks from each of 2 animals; data from 2 additional animals were not measurable due to missing toes). In (o), n = 12 for all groups (3 normal gait tracks from each of 4 animals). P values are 0.53 and 5.7×10^{-6} (m), 0.83 (n), and

0.089 and 0.0033 (o) for BBP and PDMS, respectively. Statistical significance and *P* values were determined by two-sided unpaired t-test; *$P < 0.05$; **$P \leq 0.01$; ***$P \leq 0.001$; ****$P < 0.0001$. NS; not significant.

To translate the unique mechanical advantages of the triblock BBP into practical biomedical utility, we implemented the BBP system in a peripheral nerve interface designed to communicate directly with nerve fascicles, which are enclosed by collagen-rich membranes protecting the inherent fragile nervous tissue[7,29]. Unlike other peripheral nerve implants, intraneural interfaces penetrate these collagenous membranes to access individual fascicles, enabling fascicle-specific recording and stimulation[29–32]. However, the absence of supersoft yet mechanically robust biomaterials has critically limited the utility of intraneural devices, often leading to nerve injury, fibrotic encapsulation, and progressive performance degradation[7,29]. Consequently, extraneural cuff electrodes have been more widely adopted as a safer alternative, despite their restricted access to intrafascicular structures, which prevent high-resolution neural signal capturing and fascicle-specific stimulation[30,33,34].

Our BBP network, however, meets the stringent mechanical requirements for intraneural implants. To assess chronic implant-tissue interactions, we implanted BBP and control PDMS films intraneurally into rat sciatic nerves, which experience consistent tensile and torsional stresses during normal movement and growth (Fig. 5e-g and Supplementary Figs. 37 and 38). At two weeks post-implantation, cellular responses to the triblock BBP implants were

compared to the PDMS controls (Fig. 5h). The results were consistent with subcutaneous biocompatibility (Supplementary Fig. 39). Immunohistochemical analysis revealed that BBP intraneural implants caused no significant nerve damage, whereas PDMS implants induced pronounced axonal loss at the device-tissue interface (Fig. 5i). The PDMS implants were encapsulated by activated microglia—scar tissue–forming glial cells—indicating a pronounced mechanical mismatch and neuroimmune response (Fig. 5j).

Implant-induced nerve damage and immune responses can alter both anatomy and physiology, leading to deterioration of functional performance. However, intraneural implantation of the triblock BBP met these mechanical and biological requirements: it did not affect nerve function, as evidenced by normal toe-spreading reflexes (Fig. 5k) and typical footprints comparable to healthy controls (Fig. 5l). In contrast, the stiffer PDMS caused sciatic nerve injury, accompanied by impaired toe spreading and stance. Gait analysis revealed no reduction in toe spreading during walking in the BBP group, whereas the PDMS group exhibited a significant decrease in the toe-spread index, indicating impaired stance stabilization (Fig. 5m and Supplementary Fig. 40). The overall functional score of the sciatic nerve, quantified by the Sciatic Functional Index (SFI), was comparable between BBP-implanted and healthy animals (Fig. 5n). By contrast, rats implanted with PDMS often showed behavioral abnormalities, such as skipping or missing toes—that rendered SFI unattainable, reflecting significant nerve damage. Furthermore, the normalized swing speed of the BBP-implanted hindlimb was indistinguishable from that of healthy controls, whereas the PDMS group exhibited a marked reduction in swing

speed of the implanted limb (Fig. 5o). Overall, these findings demonstrate that the tissue-like soft yet tough BBP network minimizes nerve damage even in direct contact with delicate nerve fascicles while its toughness ensures durability under physiological motion. The immune-silent integration minimized the foreign-body response and preserved nerve integrity and preserves both neural structure and function, sustaining long-term performance of the implanted nerve.

References

1. Minev, I. R. *et al.* Electronic dura mater for long-term multimodal neural interfaces. *Science* **347**, 159–163 (2015).

2. Wang, S. *et al.* Skin electronics from scalable fabrication of an intrinsically stretchable transistor array. *Nature* **555**, 83–88 (2018).

3. Kim, D.-H. *et al.* Epidermal Electronics. *Science* **333**, 838–843 (2011).

4. Yuk, H., Lu, B. & Zhao, X. Hydrogel bioelectronics. *Chem. Soc. Rev.* **48**, 1642–1667 (2019).

5. Dai, Y. *et al.* Soft hydrogel semiconductors with augmented biointeractive functions. *Science* **386**, 431–439 (2024).

6. Yuk, H., Wu, J. & Zhao, X. Hydrogel interfaces for merging humans and machines. *Nat. Rev. Mater.* **7**, 935–952 (2022).

7. Guimarães, C. F., Gasperini, L., Marques, A. P. & Reis, R. L. The stiffness of living tissues and its implications for tissue engineering. *Nat. Rev. Mater.* **5**, 351–370 (2020).

8. Patel, S. K., Malone, S., Cohen, C., Gillmor, J. R. & Colby, R. H. Elastic modulus and equilibrium swelling of poly(dimethylsiloxane) networks. *Macromolecules* **25**, 5241–5251 (1992).

9. Daniel, W. F. M. *et al.* Solvent-free, supersoft and superelastic bottlebrush melts and networks. *Nat. Mater.* **15**, 183–189 (2016).

10. Li, X. & Gong, J. P. Design principles for strong and tough hydrogels. *Nat. Rev. Mater.* **9**, 380–398 (2024).

11. Vatankhah-Varnosfaderani, M. *et al.* Mimicking biological stress–strain behaviour with synthetic elastomers. *Nature* **549**, 497–501 (2017).

12. Vatankhah-Varnosfaderani, M. *et al.* Chameleon-like elastomers with molecularly encoded strain-adaptive stiffening and coloration. *Science* **359**, 1509–1513 (2018).

13. Self, J. L. *et al.* Dynamic Bottlebrush Polymer Networks: Self-Healing in Super-Soft Materials. *J. Am. Chem. Soc.* **142**, 7567–7573 (2020).

14. Xu, P. *et al.* Conductive and elastic bottlebrush elastomers for ultrasoft electronics. *Nat. Commun.* **14**, 623 (2023).

15. Huang, B., Nian, S. & Cai, L.-H. A universal strategy for decoupling stiffness and extensibility of polymer networks. *Sci. Adv.* **10**, eadq3080 (2024).

16. Gong, J. P., Katsuyama, Y., Kurokawa, T. & Osada, Y. Double-Network Hydrogels with Extremely High Mechanical Strength. *Adv. Mater.* **15**, 1155–1158 (2003).

17. Sun, J.-Y. *et al.* Highly stretchable and tough hydrogels. *Nature* **489**, 133–136 (2012).

18. Ducrot, E., Chen, Y., Bulters, M., Sijbesma, R. P. & Creton, C. Toughening Elastomers with Sacrificial Bonds and Watching Them Break. *Science* **344**, 186–189 (2014).

19. Kang, J. *et al.* Tough and Water-Insensitive Self-Healing Elastomer for Robust Electronic Skin. *Adv. Mater.* **30**, 1706846 (2018).

20. Jung, J. *et al.* Self-healing electronic skin with high fracture strength and toughness. *Nat. Commun.* **15**, 9763 (2024).

21. Liu, C. *et al.* Tough hydrogels with rapid self-reinforcement. *Science* **372**, 1078–1081 (2021).

22. Kim, J., Zhang, G., Shi, M. & Suo, Z. Fracture, fatigue, and friction of polymers in which entanglements greatly outnumber cross-links. *Science* **374**, 212–216 (2021).

23. Steck, J., Kim, J., Kutsovsky, Y. & Suo, Z. Multiscale stress deconcentration amplifies fatigue resistance of rubber. *Nature* **624**, 303–308 (2023).

24. Xie, R. *et al.* Hydrogen-Bonding Bottlebrush Networks: Self-Healing Materials from Super-Soft to Stiff. *Macromolecules* **55**, 10513–10521 (2022).

25. Bates, C. M., Chang, A. B., Momčilović, N., Jones, S. C. & Grubbs, R. H. ABA Triblock Brush Polymers: Synthesis, Self-Assembly, Conductivity, and Rheological Properties. *Macromolecules* **48**, 4967–4973 (2015).

26. Hu, P., Madsen, J. & Skov, A. L. One reaction to make highly stretchable or extremely soft silicone elastomers from easily available materials. *Nat. Commun.* **13**, 370 (2022).

27. Tomita, S. *et al.* Coalescence of non-equilibrium spheres through thermal annealing in a polystyrene-block-poly(ethylene-co-butylene)-block-polystyrene triblock copolymer film under a uniaxially stretched state. *Polym. J.* **49**, 519–526 (2017).

28. Gu, W. *et al.* Self-Assembly of Symmetric Brush Diblock Copolymers. *ACS Nano* **7**, 2551–2558 (2013).

29. Larson, C. E. & Meng, E. A review for the peripheral nerve interface designer. *Journal of Neuroscience Methods* **332**, 108523 (2020).

30. Spearman, B. S. *et al.* Tissue-Engineered Peripheral Nerve Interfaces. *Adv. Funct. Mater.* **28**, 1701713 (2018).

31. Rodríguez-Meana, B. *et al.* Engineered Graphene Material Improves the Performance of Intraneural Peripheral Nerve Electrodes. *Adv. Sci.* **11**, 2308689 (2024).

32. Badi, M. *et al.* Intrafascicular peripheral nerve stimulation produces fine functional hand movements in primates. *Sci. Transl. Med.* **13**, eabg6463 (2021).

33. Liu, Y. *et al.* Morphing electronics enable neuromodulation in growing tissue. *Nat. Biotechnol.* **38**, 1031–1036 (2020).

34. Carnicer-Lombarte, A. *et al.* Ultraconformable cuff implants for long-term bidirectional interfacing of peripheral nerves at sub-nerve resolutions. *Nat. Commun.* **15**, 7523 (2024).

Methods

Synthetic protocols

Synthesis of bottlebrush polymer (Ring Opening Metathesis Polymerization).

A 250 mL round-bottom flask was sealed with a rubber septum, evacuated, and backfilled with argon three times. 100 mL of dry dichloromethane (DCM) was introduced and bubbled with argon for 15 minutes. In a separate 100 mL round-bottom flask equipped with a magnetic stir bar and PS macromonomer (12.0 equivalents, 0.635 g) and sealed with a septum. After three times of evacuation/argon purging cycles, dried DCM (5 mL) was added to dissolve the macromonomer under argon.

Inside a glovebox, Grubbs' third-generation catalyst (G3, 0.031 g) was weighed into a vial. The vial was taken out and subjected to three evacuation/argon purging cycles then inject 1.25 mL of dry DCM to make a stock solution.

Two additional 50 mL round-bottom flasks were prepared: one containing the PEG macromonomer (360.0 equivalents, 4.554 g) and the other containing the PS macromonomer (12.0 equivalents, 0.635g). Each flask was sealed with a septum, evacuated and purged with argon, and then charged with 40 mL and 5 mL of dry DCM, respectively.

The polymerization was initiated by injecting 0.726 mL of the G3 catalyst solution into the 100 mL flask which contains PS macromonomer and proceeded for 30 minutes (first step). The PEG macromonomer solution was then added and the reaction was continued for 1.5 hour, followed by addition of the PS macromonomer solution and further reaction for 1 hour.

The reaction was quenched by adding an excess of ethyl vinyl ether (EVE) and stirring for 10 minutes.

The crude was precipitated three times into methanol, collected, and dried under 50 ℃ vacuum to yield a viscoelastic solid.

Mechanical characterization

All uniaxial tensile and fracture tests were conducted by a universal testing machine (UTM) (Instron 68SC-1).

Uniaxial tensile test

Tensile tests were performed under ambient conditions with dogbone shape specimens. The thickness of the films was approximately 250 μm, which was measured by an optical microscope and a micrometer. The central dimension of the dogbone samples were 1.5 mm x 10 mm (width x gauge length) and the loading rate was 100 mm min^{-1} (1,000% min^{-1}).

Fracture test

Notched specimens for fracture test were prepared by cutting the polymer films into rectangular shape (40 mm x 20 mm), with the length of the notch being half of the width. The loading rate was 100 mm min^{-1} (1,000% min^{-1})

Rheology measurements

All the rheological analysis were conducted by the rheometer (Anton-paar MCR-302). 8 mm parallel plate (PP8) kit was used, and the sample was prepared by the 9 mm x 9 mm rectangle shape. Amplitude sweep test was conducted under ambient condition and the frequency was set to 1 Hz. For the TTS analysis, temperature was controlled by the peltier kit and the heating rate was 5 ℃ min^{-1} and the amplitude was set to 0.5%.

Small-angle X-ray Scattering (SAXS)

SAXS experiments were conducted at the 4C SAXS II beamline[35] located at the Pohang Accelerator Laboratory (PAL) in Pohang, Republic of Korea. Storage ring energy was 3.0 GeV, and the sample-to-detector distances were set at 4 m. To obtain 2D SAXS profiles for stretched films, a stretcher was set on the stage between the beam source and the detector. Polymer films were stretched by the stretcher and anchored on the stage and the position of the stage was controlled to ensure that the beam always pass through the middle of the specimen.

Coarse-grained model simulation (CGMS)

The ABA block copolymer is modelled as a Kremer-Grest bead-spring polymer[36,37]. All bonds between monomers are finitely extensible nonlinear elastic (FENE) bonds[37], given by equation (1), with the standard choices $k_b = 30\epsilon/\sigma^2$, $R_0 = 1.5\sigma$, $\sigma_{ij} = 1.0\sigma$, and $\epsilon_{ij} = 1.0\epsilon$, where Θ is the Heaviside step function. All simulations are performed in Lennard-Jones

(LJ) reduced units, where σ and ϵ set the units of length and energy, respectively. We set the volume fraction of A to about 0.16 to obtain spherical phase self-assembly.

$$U_{\text{bond}}(r_{ij}) = -\frac{1}{2}k_{\text{b}}R_0^2 \ln\left(1 - \left(\frac{r}{R_0}\right)^2\right) + 4\epsilon_{ij}\left(\left(\frac{\sigma_{ij}}{r_{ij}}\right)^{12} - \left(\frac{\sigma_{ij}}{r_{ij}}\right)^{6} + \frac{1}{4}\right)\Theta\left(2^{1/6}\sigma - r_{ij}\right) \quad (1)$$

For both polymer types, monomer identity is defined by the non-bonded LJ pair potential in equation (2) with a cutoff of $\text{r}_\text{c} = 3.0\sigma$. For A monomers, $\epsilon_{AA} = 3.0\epsilon$ to produce a glassy polymer. For B monomers, $\epsilon_{BB} = 1.5\epsilon$ to model a rubbery polymer. For A and B pairs, $\epsilon_{AB} = 0.5\epsilon$ to represent the incompatibility that drives phase separation in block copolymers.

$$U_{\text{pair}}(r_{ij}) = 4\epsilon_{ij}\left(\left(\frac{\sigma_{ij}}{r_{ij}}\right)^{12} - \left(\frac{\sigma_{ij}}{r_{ij}}\right)^{6} - \left(\frac{\sigma_{ij}}{r_c}\right)^{12} + \left(\frac{\sigma_{ij}}{r_c}\right)^{6}\right)\Theta(r_c - r_{ij}) \quad (2)$$

To simplify the setup, each block contains only A or only B monomers. The backbone uses a moderate angle potential that reflects the stiffness of polynorbornene or a typical glassy polymer such as polystyrene. Specifically, the cosine angle potential in equation (3) is applied to the backbone with $k_\theta = 2.0\epsilon$.

$$U_{\text{bend}}(\boldsymbol{r}_i, \boldsymbol{r}_j, \boldsymbol{r}_k) = k_\theta \left(1 + \cos \frac{\boldsymbol{r}_{jk} \cdot \boldsymbol{r}_{ji}}{|\boldsymbol{r}_{jk}||\boldsymbol{r}_{ji}|}\right) \quad (3)$$

The simulation begins from an initial configuration of 16,200 polymers randomly seeded at density $\rho = 0.85/\sigma^3$ with non-bonded interactions turned off. The desired pair potential is then introduced gradually from ideal chains over $2 \times 10^5 \tau$ to form a spherical self-assembly, where $\tau = \sqrt{m\sigma^2/\epsilon}$. Here, τ is the LJ time unit and m is the mass unit. During this pair potential recovery stage, the system is in the NPT ensemble. The temperature is held at $T = 1.0\epsilon/k_{\text{B}}$, where k_{B} is the Boltzmann constant, throughout recovery to promote formation of the spherical phase. The pressure is held at $0.0\epsilon/\sigma^3$ in all simulation. To reduce finite size effects at high strain, the simulation cell is set to an anisotropic shape with $L_{yz}/L_x = 6\sqrt{2}$, where x is the uniaxial deformation direction, so the cell keeps a moderate aspect ratio even at high strain.

After recovery, the temperature is set to $T = 0.8\epsilon/k_{\text{B}}$ for a short equilibration ($\sim O(10^4)\tau$) before deformation and is then maintained during deformation. The strain rate is kept constant at $5 \times 10^{-5}/\tau$, and deformation is applied at every timestep.

All simulations were performed with Large-scale Atomic/Molecular Massively Parallel Simulator (LAMMPS)[38].

Biological analysis

In vivo implantation

All animal surgeries were conducted under approval of Institutional Animal Care and Use Committee at Seoul National University Hospital (Approval number: SNU-250115-4). 6-week female Sprague Dawley rats (Koatech) were used for all in vivo implantation studies. The polymer implant samples were prepared using sterile techniques and further sterilized by immersing 100% Ethanol for 1h. Animals were anesthetized with isoflurane (4-5% induction, 2-3% maintenance) for implantation surgery. For implantation of intraneural implants in sciatic nerve, hindlimb hair was removed and skin was sterilized with betadine. A 2-cm incision in skin and fascia was made carefully. Proximal sciatic nerves were transposed, and careful nerve incision was made with fine surgical forceps (11241-30, Dumont) for intraneural implantation of polymer film (20 mm (L) X 1.5mm (W) X 250 μm (T)). The proximal end of the intraneural implant is connected to PDMS connector (30 mm (L) X 3mm (W) X 300 μm (T)), anchored to the L4-5 vertebrae with superbond (C&B super bond, Sun Medical) and dental cement (Self-curing, Vertex dental). The distal end of the intraneural implant was sealed with Kwik-Sil to prevent the implant dislocation. The surgical sham group underwent aforementioned surgery without polymer implantation. For implantation of subcutaneous implants, back hair was removed, and skin was sterilized with betadine. A 1-cm skin incision was made and polymer films (5mm (L) X 5mm (W) X 800 μm (T)) were inserted in subcutaneous pocket. Following implantation, the surgical sites were irrigated with sterile saline and closed using 6-0 Vicryl and 5-0 Black silk sutures (Ethicon). After 2 weeks of implantation, the histology samples were harvested under anesthesia and animals were euthanized by CO2 inhalation.

Acknowledgements

This study was supported by the Nano & Material Technology Development Program through the National Research Foundation of Korea (NRF) funded by Ministry of Science and ICT (NRF grants RS-2024-00402972), Global Bio-Integrated Materials Center (RS- 2024-00406240) and Boston-Korea Project (RS-2024-00467213). I.L. and C.M.B. thank the National Science Foundation (CMMI-2053760) for support and the BioPACIFIC Materials Innovation Platform (DMR-2445868) for instrumentation. B.L. acknowledges support from the U.S. DOE Office of Science-Basic Energy Sciences, under Contract No. DEAC02-06CH11357.

Author Contributions

H.K., C.M.B. and J.K. conceived and designed the experiments. H.K., J.L., and I.L. synthesized and optimized bottlebrush polymers. H.K. performed mechanical properties analysis and studied mechanism. H.K. and B.L. studied network structure through SAXS analysis. J.W.Y. and Y.J.K. performed CGMD simulations. Y.S. and S.P. designed and conducted biological tests. H.K., Y.S., J.W.Y., S.P. and J.K. wrote the paper. All the authors discussed the results and commented on the manuscript. J.K. supervised the study.

Competing Interests

The authors declare no competing interest.

References

35. Kim, K.-W. *et al.* Small-angle X-ray scattering beamline BL4C SAXS at Pohang Light Source II. *BioDesign* **5**, 24–29 (2017).

36. Grest, G. S. & Kremer, K. Molecular dynamics simulation for polymers in the presence of a heat bath. *Phys. Rev. A* **33**, 3628–3631 (1986).

37. Kremer, K. & Grest, G. S. Dynamics of entangled linear polymer melts: A molecular-dynamics simulation. *J. Chem. Phys.* **92**, 5057–5086 (1990).

38. Thompson, A. P. *et al.* LAMMPS - a flexible simulation tool for particle-based materials modeling at the atomic, meso, and continuum scales. *Comput. Phys. Commun.* **271**, 108171 (2022).

Supplementary Files

This is a list of supplementary files associated with this preprint. Click to download.

- SupplementaryVideo1.mp4
- KimSI.pdf